Development of Heat Transfer Correlations for LOX/CH4 Thrust Chambers

B. Betti[⋆,†], *D. Liuzzi*[⋆⋆], *F. Nasuti*[⋆] *and M. Onofri*[⋆]

[⋆] *"Sapienza" University of Rome, via Eudossiana 18, 00186, Rome, Italy.*
[⋆⋆]*Avio S.p.a., via Ariana km 5.2, 00034 Colleferro (RM), Italy*

[†] Corresponding author: barbara.betti@uniroma1.it

Abstract

The evaluation of the convective heat transfer coefficient is one of the key point to design an efficient liquid rocket engine thrust chamber. In order to reduce the computational cost during the preliminary analysis, engineering tools are preferred provided that they are used within their calibration range. In this framework, Bartz's equation is calibrated to match CFD results of the LM10-MIRA oxygen/methane thrust chamber in different operating conditions and including the effect of axial wall ribs. The specifically calibrated version of Bartz's equation provides a good evaluation of the convective heat transfer coefficient in the range of wall temperature, chamber pressure and mixture ratio investigated and in the case of axial wall ribs with different heights.

1. Introduction

In liquid rocket engine thrust chambers, the hot gas flow reaches very high temperatures which exceed by far the safe temperature limit of metallic materials, hence requiring active cooling to preserve the walls from mechanical failure. In regeneratively cooled thrust chambers, which are characterized by low wall temperatures, strong thermal gradients establish between the hot combustion products (>3000 K) and the wall, whose maximum allowed temperature is lower than 850 K for the best material.[1] Therefore, thermal analysis is fundamental to guarantee safe operation while reducing mass and volumes. In the design phase, reduced order models are widely adopted to compare different configurations and evaluate the performance of the complete system with a low computational cost. These models come from the studies on thermal boundary layers, which have been performed in depth since '50s, to identify the main physical phenomena that drive the heat transfer from hot gas to the wall.[2] Studies have been mainly devoted to collect experimental measurements and to derive semi-empirical correlations for the convective heat transfer coefficient. The goal was to measure the convective heat transfer coefficient in different conditions and describe the behavior observed in the experimental tests making it easy to use as design tool.[3,4] In the study of thrust chamber heat transfer, the same approach led to the development of the widely used semi-empirical correlation referred to as Bartz's equation. Nevertheless, care must be taken in using semi-empirical correlations outside their calibration range. To avoid this kind of risks or inaccuracies, a possible approach is that once a basic thrust chamber configuration is selected, semi-empirical correlations are inspected and possibly recalibrated with the help of CFD simulations.

Being the methane a possible cheaper and denser replacement of hydrogen in launch vehicles,[5] the aim of the present work is to extend the Bartz's equation heat transfer correlation to oxygen/methane thrust chambers including the aspects related to the strong gradients involved in the flow evolution from the combustion chamber to the nozzle exit and the effect of axial ribs on the hot-gas side. The calibration is focused on the LM10-MIRA oxygen/methane thrust chamber geometry and its nominal load point.[6]

2. Numerical method and approach

A Reynolds-Averaged Navier-Stokes (RANS) approach is used to obtain CFD solutions of the hot-gas flow-field and heat transfer in the thrust chamber. The steady state numerical solutions are carried out by means of an in-house finite volume RANS equations solver, second order accurate in space, able to treat multi-component mixtures of thermally perfect gases which can evolve in the flow-field according to a finite-rate chemical reaction mechanism. Time integration is done using the Strang operator-splitting technique.[7] The convective and diffusive terms are integrated using a second order accurate Runge-Kutta scheme while the chemical source term is integrated using a stiff ode implicit integrator.[8] Turbulence is described by means of the Spalart-Allmaras one-equation model,[9] a constant turbulent Schmidt number is adopted to model turbulent diffusivity and a constant turbulent Prandtl number is adopted to model turbulent conductivity. Gas thermodynamic and transport properties as well as chemical kinetic rates are evaluated as a function of the local temperature and composition.[10] The values are evaluated for each species at different temperatures and stored in look-up tables to reduce the computational cost of each time step. The mixture value of the thermodynamic properties is evaluated as the weighted sum of the value of each species by means of the species mass fraction. The mixture value of the transport properties is evaluated by means of the Wilke's mixing rule.[11] The present solver has been validated against experimental data[12–15] in different test cases.

Neglecting injection and flame details is a reasonable simplification for the goals of the present study. In full scale engines and sufficiently downstream of the injector plate, this assumption gives solutions in agreement with the results obtained with more complex approaches, which take into account for the phenomena involved in the propellant injection and combustion.[12,14] Hence, this simplification is adopted in the present analysis bearing in mind that, because of the lack of modeling of the near injector plate phenomena, the evaluation of heat transfer in the vicinity of the injector plate is not reliable.

In the CFD solution, wall heat flux is evaluated as the conductive heat transfer between the fluid and the wall, where the fluid is characterized by zero velocity. Wall heat flux can be expressed by the Fourier's law as the product of the thermal conductivity k and the temperature gradient normal to the wall: $q_w = k\,(\nabla T)_n$. The wall is supposed to be non-catalytic, hence no species mass fraction gradient contribution has to be added to the wall heat flux evaluation.

2.1 Chemical kinetic schemes

When dealing with hydrocarbon fuels, the combustion involves a large number of intermediate products and reactions. Despite methane is the simplest hydrocarbon, the number of species to take into account for a detailed description of the combustion process is large, increasing dramatically the computational cost associated to a CFD simulation of a full scale engine. In this frame, exploiting global reaction mechanisms, which are still able to provide a sufficient description with a reduced number of species, can become of great interest.

To describe the finite-rate chemistry of the oxygen/methane combustion, an extension of the Jones-Lindstedt global mechanism including the dissociation/recombination reactions of O_2 and H_2O (JL-R)[16] is selected, that comprises 9 species and 6 reactions. The comparison of the solution obtained by the selected model and a detailed mechanism showed that it is able to reliably reproduce the main recombination reactions inside the thermal boundary layer with a reduced computational cost.[17] Being interested in near wall reactions starting from equilibrium combustion products, the global mechanism has been further simplified. Noting that methane is not present as a combustion product in the thrust chamber because of the high temperature, even if it is a fuel rich environment, methane is not taken into account as a species in the present simulations because it is involved only in irreversible reactions. This further simplification reduces the JL-R mechanism to 8 species (H, H_2, H_2O, O, O_2, OH, CO, CO_2) and 4 reversible reactions as summarized in Table 1.

Reactions						Rates
CO	+	H_2O	$\rightleftharpoons$	CO_2	+ H_2	$r_1 = 2.75 \cdot 10^9 e^{-\frac{20000}{RT}}\,[CO]\,[H_2O]$
H_2	+	$\frac{1}{2}\,O_2$	$\rightleftharpoons$	H_2O		$r_2 = 6.80 \cdot 10^{15} T^{-1} e^{-\frac{40000}{RT}}\,[H_2]^{0.25}\,[O_2]^{1.50}$
		O_2	$\rightleftharpoons$	2O		$r_3 = 1.5 \cdot 10^9 e^{-\frac{113000}{RT}}\,[O_2]$
		H_2O	$\rightleftharpoons$	H	+ OH	$r_4 = 2.3 \cdot 10^{22} T^{-3} e^{-\frac{120000}{RT}}\,[H_2O]$

Table 1: JL-R model reactions (units: cal, mol, l, s)[16] .

2.2 Numerical grid and boundary conditions

The computational domain within the LM10-MIRA thrust chamber without axial wall ribs is discretized by means of a 2D axis-symmetric structured grid. Volumes are clustered toward the wall in the radial direction to properly solve the viscous sublayer of the boundary layer. The numerical grid and the boundary conditions enforced are shown in Fig. 1.

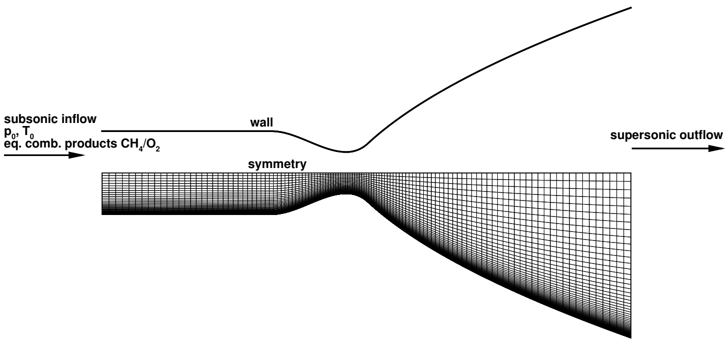

Figure 1: Computational domain: numerical grid (bottom) and boundary conditions (top).

A symmetry condition is applied to the centerline. At the chamber wall boundary, no-slip and non-catalytic conditions are applied prescribing the wall temperature. Enforcing the experimental wall temperature as numerical boundary condition, the numerical wall heat flux is computed. An extrapolated exit boundary condition is used to simulate the supersonic outflow at the nozzle exit. The left boundary of the domain is a subsonic inflow where stagnation pressure and stagnation temperature are prescribed together with the velocity direction and the mixture inlet composition. The chamber pressure is applied as the inlet stagnation pressure. The inlet stagnation temperature is the adiabatic flame temperature evaluated, together with the mixture inlet composition, by means of the "Chemical Equilibrium and Applications" (CEA) program,[18] under the assumption of chemical equilibrium at the chamber pressure and mixture ratio. The injected mixture composition varies inside the thrust chamber according to the JL-R finite-rate chemical kinetic mechanism.

In addition, in order to include the ribbed walls in the cylindrical section, a 3D slice of the chamber is discretized including half a rib and half the empty space between two ribs. The boundary conditions are the same as those shown in Fig. 1 extended to the 3D case. In the spanwise and radial directions, volumes are clustered toward the walls in the cylindrical section to solve the viscous region within two ribs.

2.2.1 Grid convergence

In order to verify grid independence and evaluate the numerical error, the solutions obtained with three different levels of refinement of the domain discretization are compared in the frozen flow condition with oxygen/methane. The finer grid mesh is composed by 240×160 volumes in axial and radial direction, respectively. The medium grid mesh is obtained from the finer grid mesh halving the volumes in both axial and radial directions. The coarse grid is obtained from the medium, similarly. The numerical error is evaluated comparing each grid solution to the Richardson extrapolated solution[19] computed as:

$$f_{RE} = f_{fine} + \frac{f_{fine} - f_{medium}}{r^2 - 1} \tag{1}$$

where f_{RE}, f_{fine} and f_{medium} are the extrapolated solution, the fine solution, and the medium solution, respectively, and r is the spatial order of accuracy of the solver.

In Fig. 2, the Richardson extrapolated wall heat flux is shown along the thrust chamber. In the cylindrical section, the simplifying assumption of injecting the equilibrium combustion product mixture provides a decreasing trend related to the development of the boundary layer on the wall. In the throat region, the wall heat flux shows a maximum related to the minimum surface of the chamber wall and the acceleration of the flow. In the divergent section, the wall heat flux decreases because the contribution of the acceleration of the flow to the convective heat transfer is dumped by the increasing wall surface. In this region, the two different slopes of the wall heat flux decreasing trend can be associated to the change of concavity of the profile.

The three grids are designed to provide a non-dimensional wall distance of the order of 1 in the throat region for all the refinement levels.

In Fig. 2 the numerical error along the thrust chamber is also shown for the three grid levels compared to the Richardson extrapolated solution. In particular, neglecting the near injector plate region, the numerical error related to the medium grid level is less than 2% with respect to the Richardson extrapolated solution of the wall heat flux. In the following, the medium grid, made of 120×80 volumes, has been therefore selected for the parametric analysis.

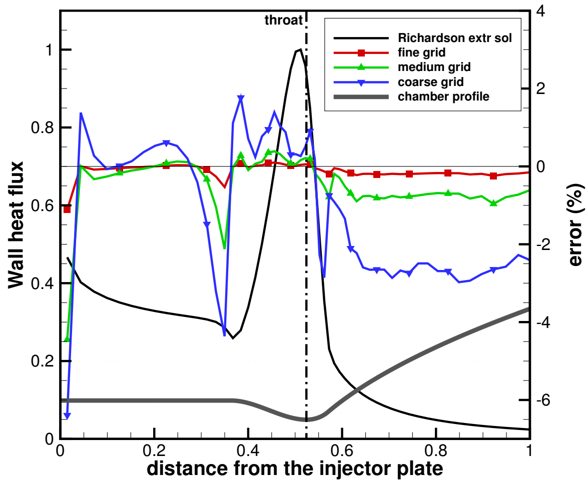

Figure 2: Richardson extrapolated solution for wall heat flux and numerical error associated to three grid levels.

3. Parametric analysis

The nominal load point of the engine is assumed as a starting point to investigate the influence of wall temperature, chamber pressure, and chamber mixture ratio on the prediction of wall heat flux. Each parameter is varied while keeping the others constant at their nominal point value as summarized in Table 2. In addition, rib height h_{rib} is varied with respect to the chamber thickness t in order to evaluate the rib efficiency in increasing the heat transfer from the hot gas to the wall.

Run	Description	T_w (K)	p_c (bar)	O/F	h_{rib}/t
1	**Nominal load point**	**800**	**60**	**3.4**	**0.0**
2	T_w variation	**600**	60	3.4	0.0
3	”	**1000**	60	3.4	0.0
4	p_c variation	800	**40**	3.4	0.0
5	”	800	**80**	3.4	0.0
6	O/F variation	800	60	**3.1**	0.0
7	”	800	60	**3.7**	0.0
8	h_{rib} variation	800	60	3.4	**0.25**
9	”	800	60	3.4	**0.50**
10	”	800	60	3.4	**0.75**
11	”	800	60	3.4	**1.00**

Table 2: Parametric analysis test matrix.

To compare the numerical results with those obtained with the Bartz's correlation, the heat transfer coefficient is evaluated starting from the numerical wall heat flux:

$$\left(h_{c,hg}\right)_{CFD} = \frac{(q_w)_{CFD}}{T_{aw} - T_w} \tag{2}$$

where T_{aw} is the adiabatic wall temperature. Being here a reference value, T_{aw} is assumed as the temperature related to the adiabatic wall enthalpy evaluated with the CEA program[18] for each load point at each section under the Bray hypothesis[20] for the flow evolution inside the nozzle: chemical equilibrium up to the throat and then frozen mixture composition in the divergent section. In addition, for each section, chemical equilibrium inside the boundary layer is assumed.

The first hypothesis is related to the residence time inside the nozzle and the Damköhler number Da order of magnitude along the nozzle: in the combustion chamber up to the convergent section, the reaction rates are faster than the convective mass transport rates (i.e. $Da >> 1$ hence chemical equilibrium). From the throat downstream, the flow rapidly accelerates and reaction rates become slower than the convective transport rates (i.e. $Da << 1$ hence frozen flow). The second assumption is related to the fact that inside the boundary layer, despite the external chemical model (i.e. chemical equilibrium or frozen flow), the flow mixture composition behaves as in chemical equilibrium being here the flow velocity near zero.

The adiabatic wall temperature assumed in the evaluation of the convective heat transfer coefficient in the nominal load point is shown in Fig. 3 along the nozzle.

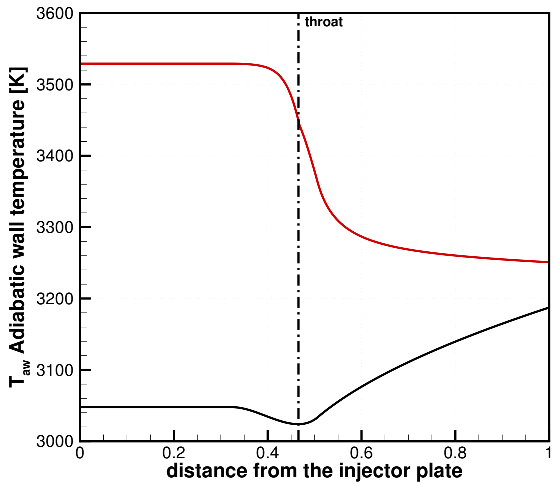

Figure 3: Reference adiabatic wall temperature along the nozzle.

3.1 Effect of varying wall temperature

The effects of wall temperature on heat transfer are investigated in runs 2 and 3 with respect to the nominal load point. The three test cases differ in the wall temperature enforced at the wall as boundary condition. In Fig. 4(a), CFD numerical solutions of runs 1 to 3 are shown in terms of heat transfer coefficient along the nozzle evaluated by means of Eq. 2 where T_{aw} is that shown in Fig. 3.

Increasing the wall temperature results in a slight increase of the heat transfer coefficient. Moreover, the effect of this increase on the wall heat flux is negligible because of the direct dependence of q_w on T_w in Eq. 2. Wall temperature effects on heat transfer coefficient are more pronounced in the cylindrical section of the chamber up to the throat. Downstream of the throat, heat transfer coefficient shows negligible differences varying wall temperature. This can be ascribed to the fact that in the cylindrical section, near wall recombination affects the composition of the mixture inside the boundary layer more than in the divergent part. This is related to two causes: the presence in the core flow of larger mass fractions of dissociated species in the cylindrical section and a decreasing temperature of the core flow from the cylindrical section to the divergent section caused by the expansion through the nozzle.

3.2 Effect of varying chamber pressure

The effect of the variation of chamber pressure on wall heat flux in the numerical simulations is investigated in runs 4 and 5 with respect to the nominal load point. The three test cases differ in terms of stagnation pressure and temperature, and the mixture composition enforced at the subsonic inflow, as summarized in Table 3. Increasing chamber pressure, the adiabatic flame temperature, which is assumed as the stagnation temperature, increases and the mass fraction of the dissociated species decreases in favor of the presence of recombined species.

As shown in Fig. 4(b), the result is the expected increase of the convective heat transfer coefficient along the whole nozzle for increasing chamber pressure. In particular this is more visible in the cylindrical section and in the throat region.

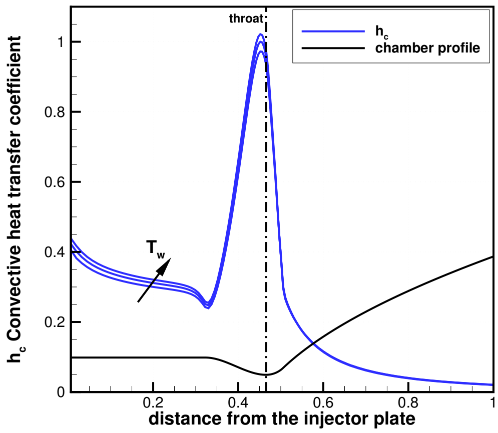

(a) Wall temperature effect.

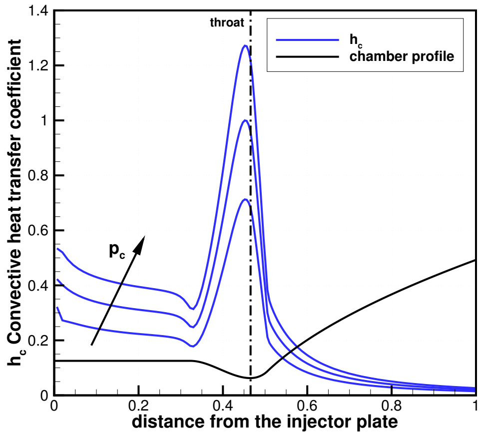

(b) Chamber pressure effect.

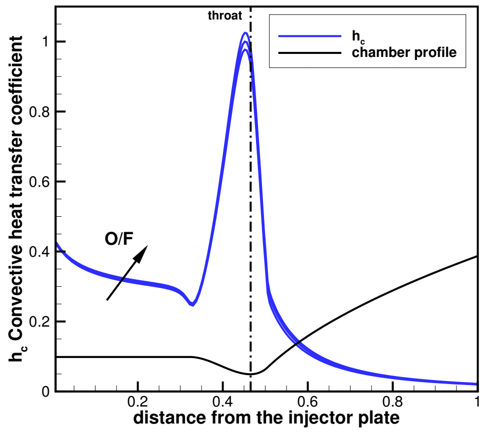

(c) Mixture ratio effect.

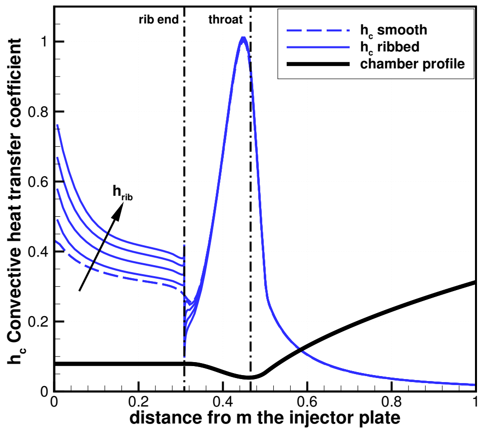

(d) Rib height effect.

Figure 4: Convective heat transfer coefficient along the chamber wall.

Run	p_0 (bar)	T_0 (K)	Mixture composition (mass fraction)							
			H	H_2	H_2O	O	O_2	OH	CO	CO_2
4	40	3540.73	0.0014	0.0084	0.3884	0.0111	0.0438	0.0635	0.2453	0.2380
1	60	3598.04	0.0013	0.0082	0.3925	0.0101	0.0412	0.0618	0.2426	0.2422
5	80	3638.85	0.0012	0.0080	0.3995	0.0093	0.0393	0.0605	0.2406	0.2454

Table 3: Subsonic inflow details varying chamber pressure.

3.3 Effect of varying mixture ratio

The effect of the variation of chamber mixture ratio on the wall heat flux is investigated in runs 6 and 7 with respect to the nominal load point. The three test cases differ in terms of stagnation temperature and mixture composition enforced at the subsonic inflow, as summarized in Table 4

Being interested in fuel rich test cases, increasing the mixture ratio means to move toward the stoichiometric mixture ratio where the adiabatic flame temperature reaches its maximum value.

Fig. 4(c) shows that the heat transfer coefficient is slightly affected by the mixture ratio variation: the difference between the three runs is only visible in the maximum value in the throat.

Run	p_0 (bar)	T_0 (K)	Mixture composition (mass fraction)							
			H	H_2	H_2O	O	O_2	OH	CO	CO_2
6	60	3557.62	0.0014	0.0114	0.4067	0.0064	0.0198	0.0498	0.2882	0.2163
1	60	3598.04	0.0013	0.0082	0.3925	0.0101	0.0412	0.0618	0.2426	0.2422
7	60	3608.57	0.0011	0.0062	0.3759	0.0130	0.0682	0.0691	0.2053	0.2611

Table 4: Subsonic inflow details varying chamber mixture ratio.

3.4 Effect of varying the rib height

Being the cylindrical section of the engine provided of longitudinal wall ribs, the heat transfer enhancement related to the surface increase has been investigated varying the height of the ribs keeping their number constant. The characteristic height of the rib is lower than the boundary layer thickness, hence they are completely immersed in the boundary layer. In Fig. 4(d), the convective heat transfer coefficient in case of ribbed wall with increasing rib height is compared to the smooth reference test case.

The convective heat transfer coefficient is larger in the cylindrical section where the wall ribs are placed but does not change in the nozzle downstream of the ribs end. This result can be ascribed to their small height with respect to the thrust chamber dimensions. As expected, the heat transfer coefficient increases with increasing rib height, because of the associated surface increase. Moreover, the increase of heat transfer is proportional to the rib height, as shown in Fig. 5, comparing the heat transfer with wall ribs and the smooth wall test case $\Delta h_c = h_{c,\,rib} - h_{c,\,smooth}$

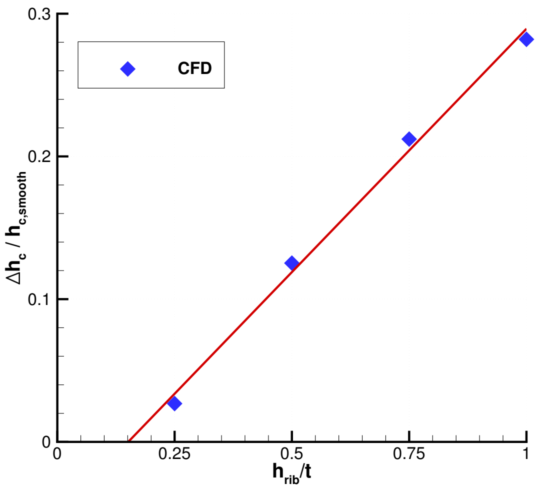

Figure 5: Convective heat transfer enhancement in case of ribbed wall.

4. Semi-empirical correlation

As a starting point to evaluate the heat transfer coefficient by means of a semi-empirical correlation, several equations have been identified. One of the most used correlations is the Bartz's equation[21] that provides the convective heat transfer coefficient depending on chamber flow properties and geometry:

$$\left(h_{c,hg}\right)_{Bartz} = \frac{0.026}{D_*^{0.2}}\left(\frac{\mu^{0.2}c_p}{Pr^{0.6}}\right)\left(\frac{p_c}{c^*}\right)^{0.8}\left(\frac{A_*}{A}\right)^{0.9}\left(\frac{D_*}{r_c}\right)^{0.1}\sigma \tag{3}$$

where D_* is the throat diameter and r_c its radius of curvature, μ is the viscosity, c_p is the specific heat, Pr is the Prandtl number, p_c is the chamber pressure, c^* is the characteristic velocity, and A_*/A is the area ratio between the throat and each section. All values are computed at the chamber conditions. The temperature corrective factor σ takes into account the strong thermal gradient inside the chamber related to the cooled walls and the presence of combustion products:

$$\sigma = \frac{1}{\left[\frac{1}{2}\left(\frac{T_w}{T_0}\right)\left(1+\frac{\gamma-1}{2}M^2\right)+\frac{1}{2}\right]^{0.8-m/5}\left[1+\frac{\gamma-1}{2}M^2\right]^{m/5}} \tag{4}$$

where m is the exponent of the viscosity dependance on temperature (i.e. m=0.6), T_w is the wall temperature, T_0 is the adiabatic flame temperature in the chamber, M is the Mach number at the section and γ is the specific heat ratio at the chamber conditions.

Other empirical correlations such as Pavli's,[22] Cinjarev's[23] and Krueger's[24] and Schacht's[25] equations are given in terms of the Stanton number St defined as the ratio between the Nusselt number and the product of Reynolds and Prandtl numbers: $St = Nu/(Re\ Pr)$. The different correlations have the same general form depending on Re, Pr and a temperature correction to take into account for the large gradient between the hot core and the wall, which is a peculiar aspect of the regeneratively cooled thrust chambers:

$$St = \mathbf{C}\ Re^{\alpha}\ Pr^{\beta}\left(\frac{T_{hot}}{T_{ref}}\right)^{\gamma} \tag{5}$$

where the constant **C** and the exponents α, β and γ vary together with the reference temperature and the reference length assumed. The coefficients for the Stanton type correlations described by Eq. 5 are summarized in Table 5, where T_{aw} is the adiabatic wall temperature, T_∞ is the core flow temperature, T_w is the wall temperature and T_0 is the stagnation temperature inside the chamber.

Equation	Ref	**C**	α	β	γ	T_{hot}	T_{ref}
Pavli	[22]	0.0230	-0.2	-0.6	0.8	T_{aw}	$(T_{aw}+T_w)/2$
Cinjarev	[23]	0.0162	-0.18	-0.18	0.35	T_{aw}	T_w
Krueger	[24]	0.0307	-0.2	-0.667	0.8	T_∞	T_{Eckert} *
Schacht	[25]	0.0215	-0.2**	-0.7	0	-	-

* $T_{Eckert} = \frac{T_w + T_\infty}{2} + 0.22\sqrt[3]{Pr}\,(T_0 - T_\infty)$

** exponent for Re_x

Table 5: Coefficients for Stanton type correlations.

In the following, only Bartz's equation has been considered and it is used as the starting point for the calibration made to match the numerical solution. The comparison of the heat transfer coefficient evaluated with Eq. 3 and by means of Eq. 2 starting from the CFD solution is shown in Fig. 6 for the nominal load point (run 1).

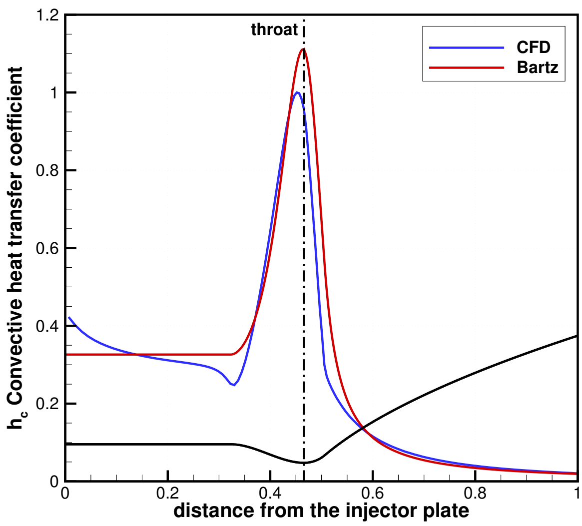

Figure 6: Comparison between Bartz's heat transfer coefficient (Eq. 3) and CFD numerical solution (Eq. 2) for the nominal load point (run 1).

In particular, the result given by the Bartz's correlation differs from the CFD numerical solution in the following regions: the cylindrical section, the throat region and the divergent part of the nozzle. In the first, Bartz's equation is based on the local area ratio and does not take into account for the development of the boundary layer and hence its increasing thickness. This assumption results in a constant value of h_c in contrast with the numerical solution. Moreover, it does not include the wall ribs contribution as heat transfer enhancement devices. In the throat region, the maximum value of the heat transfer coefficient evaluated by means of the Bartz's equation is in the throat section, whereas the CFD numerical simulation, taking into account for the two dimensional flow in the nozzle, shows the maximum heat transfer coefficient value slightly before the throat. Moreover, the peak value is overestimated with respect to the numerical simulation. In the divergent part of the nozzle, Bartz's equation does not reproduce the two different slopes in the decreasing trend associated to the expansion fan origin located in the change of concavity of the wall.

Despite these differences Bartz's equation results can provide a conservative evaluation of the heat transfer coefficient in all the test cases of the parametric analysis as can be observed in Fig. 7(a) for the wall temperature variation, in Fig. 7(b) for the chamber pressure and in Fig. 7(c) for the chamber mixture ratio.

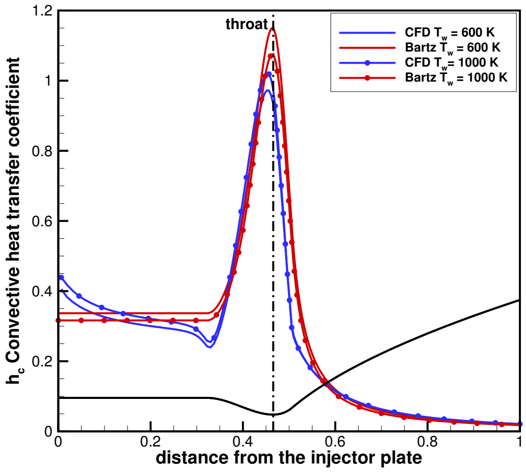

(a) Wall temperature variation.

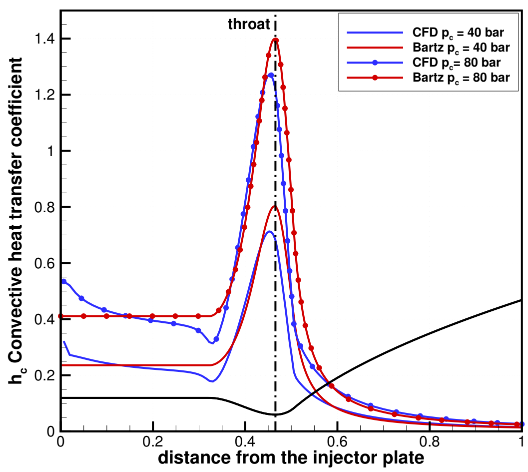

(b) Chamber pressure variation.

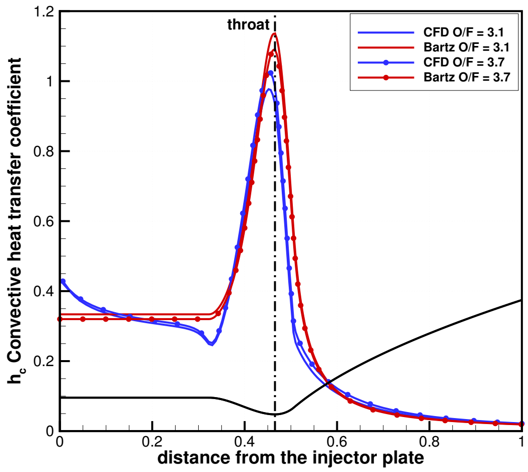

(c) Mixture ratio variation.

Figure 7: Comparison between Bartz's heat transfer coefficient (Eq. 3) and CFD numerical solution (Eq. 2).

The heat transfer coefficient evaluated by means of Bartz's equation slightly decreases with increasing wall temperature. In fact, the correlation takes into account the wall temperature only inside the temperature correction factor σ (Eq. 4) which decreases with increasing wall temperature.

Varying the chamber pressure, the difference of the heat transfer coefficient between the Bartz's equation solution and the numerical evaluation remains constant, which is an index of the efficient reduction of the chamber pressure influence inside the correlation.

In Bartz's equation, chamber mixture ratio is taken into account implicitly inside the flow properties at the chamber conditions as μ, Pr, c^* and in T_0 included in the σ coefficient. The result is a slight decrease of the heat transfer coefficient with increasing mixture ratio in the fuel rich regime. In both variation of wall temperature and mixture ratio, the CFD numerical simulations show an opposite trend with respect to the Bartz's equation solution.

Nevertheless, it is worth noting that the convective heat transfer coefficient is defined in order to combine the cause/effect relationship between wall temperature and wall heat flux, hence very small variations are expected when varying wall temperature. The extent of the variations is well captured by numerical simulations as well as by Bartz's equation. On the other hand, the mixture ratio range variation is confined in the fuel rich regime, hence providing small variations in the combustion products composition and adiabatic flame temperature. As a consequence, the effects on the heat transfer coefficient are very limited as captured by both numerical simulations and Bartz's equation solution.

In case of wall ribs, Bartz's equation does not include the heat transfer enhancement related to the surface increase, hence it is not able to provide a prediction of the convective heat transfer coefficient in this configuration.

4.1 Calibration

In order to extend the validity of the Bartz's equation to the present test matrix, a calibration has been performed in three steps. First, the heat transfer coefficient maximum value is calibrated starting from Eq. 3 to match the value of the CFD results. Then, from the analysis of the numerical heat transfer coefficient profile, two additional terms, related to geometrical features of the thrust chamber profile, are added to match the peculiar shape of the coefficient in the cylindrical section and in the throat region. Finally, the enhancement effect of wall ribs is included. The correction has the form shown in Eq. 6.

$$\left(h_{c,hg}\right)_{corr} = \left(h_{c,hg}\right)_{Bartz} \underbrace{\mathbf{C}\left(\frac{T_w}{T_{w,nom}}\right)^{\alpha}\left(\frac{p_c}{p_{c,nom}}\right)^{\beta}\left(\frac{OF}{OF_{nom}}\right)^{\gamma}}_{maximum\ value\ calibration} \underbrace{\left(\frac{x}{x_*}\right)^{\delta}\left(1-\frac{dr}{dx}\right)^{\epsilon}}_{geometry} \underbrace{\left(1+\zeta\frac{h_{rib}}{t}\right)}_{rib\ effect} \tag{6}$$

where the reference values are those of the nominal load point:

$$T_{w,nom} = 800\ K \ , \ \ p_{c,nom} = 60\ bar \ , \ \ OF_{nom} = 3.4 \ ,$$

x is the distance from the injector plate, x_* is the distance of the throat from the injector plate, dr/dx is the profile gradient in each section.

The difference between the CFD numerical results and the values provided by Bartz's equation and its calibrated version are summarized in Table 6 in terms of percentage error with respect to the CFD numerical value. With the proposed correction, the error on the maximum value is decreased from a maximum value of +16.30% in the Bartz's evaluation to a maximum value of +0.45% with the calibrated version.

Run	Load point				$\Delta h_{c,hg}$ [%]	
	T_w (K)	p_c (bar)	OF	h_{rib}/t	Bartz (Eq. 3)	Calibrated (Eq. 6)
1	800	60	3.4	0.0	11.15	-0.01
2	600	60	3.4	0.0	18.34	0.13
3	1000	60	3.4	0.0	5.27	0.45
4	800	40	3.4	0.0	12.66	-0.14
5	800	80	3.4	0.0	10.08	0.10
6	800	60	3.1	0.0	16.30	0.06
7	800	60	3.7	0.0	6.39	0.15
8	800	60	3.4	0.25	11.15	-0.01
9	800	60	3.4	0.50	11.15	-0.01
10	800	60	3.4	0.75	11.15	-0.01
11	800	60	3.4	1.00	11.15	-0.01

Table 6: Peak value of the heat transfer coefficient: percentage error with respect to the CFD numerical value.

The evolution of the heat transfer coefficient along the thrust chamber obtained by means of the numerical simulation, the Bartz's equation and its calibrated version is shown in Fig. 8 for the nominal load point (run 1).

In addition to the maximum value tuning, the trend along the chamber is better reproduced by the calibrated version of the correlation. In the cylindrical section, the decreasing trend is reproduced taking into account for the

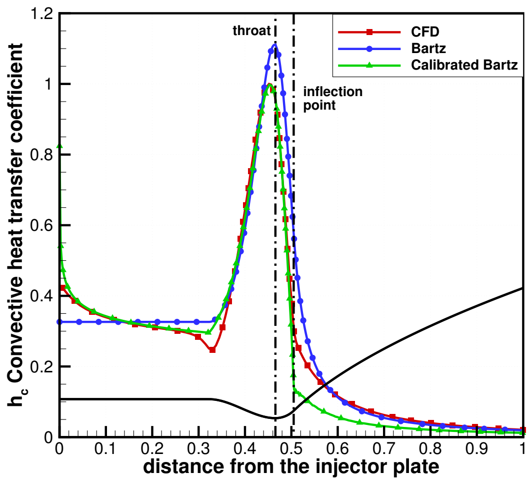

Figure 8: Comparison between CFD numerical solution (Eq. 2), Bartz's heat transfer coefficient (Eq. 3) and its calibrated version (Eq. 6) for the nominal load point (run 1).

increasing thickness of the developing boundary layer. Moreover, the rib effect is included by means of the rib efficiency associated to the surface increase. Introducing the geometrical effect related to the local slope of the profile, the shape of the peak is reproduced with a very good agreement including the position of the maximum value slightly upstream of the geometrical throat. The different slope in the divergent section is reproduced, nevertheless the correlation can be further refined to match here the numerical solution value.

The calibrated correlation is able to provide the heat transfer coefficient along the thrust chamber in very good agreement with the numerical solution in all the load points as shown in Figs. 9(a) for the variation of the wall temperature, in Figs. 9(b) for the variation of the chamber pressure and in Figs. 9(c) for the chamber mixture ratio. Moreover, in case of ribbed walls in the cylindrical section, heat transfer enhancement contribution is included and the results are shown in Figs. 9(d). Neglecting the near injector plate region, where both numerical solution and correlations are not accurate, the calibrated version is in good agreement with the numerical solution.

5. Conclusions

RANS numerical simulations have been used to provide a test matrix by means of a parametric analysis to investigate the capability of Bartz's correlation for heat transfer coefficient evaluation in different operative conditions. Having as a goal to match the numerical solution, a calibrated version of the Bartz's equation is discussed to reproduce the maximum value of the numerical heat transfer coefficient and its evolution along the thrust chamber. Very good agreement is achieved in all the thrust chamber sections in terms of trend and values. Further refinement can provide a better value agreement in the divergent region. In case the cylindrical section is equipped with axial ribs, the heat transfer enhancement due to the presence of these devices has to be taken into account. This contribution is included by means of the rib efficiency as a function of the surface increase provided by the wall ribs.

Acknowledgments

The present study has been carried out with the support of the Italian Space Agency (ASI).

References

[1] Sutton, G. and Biblarz, O., *Rocket propulsion elements*, John Wiley & Sons, 2001.

[2] Spalding, D., "Heat transfer from chemically reacting gases," *Modern Developments in Heat Transfer*, Vol. 1, Academic Press, 1963, pp. 19–64.

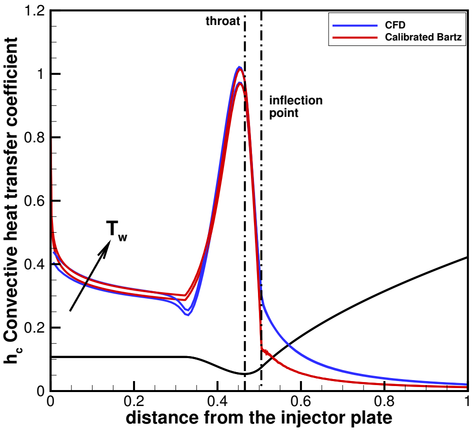

(a) Wall temperature variation.

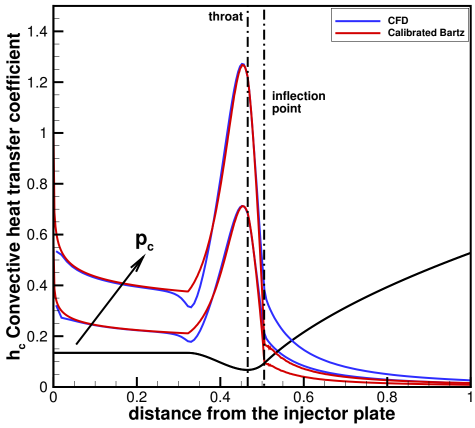

(b) Chamber pressure variation.

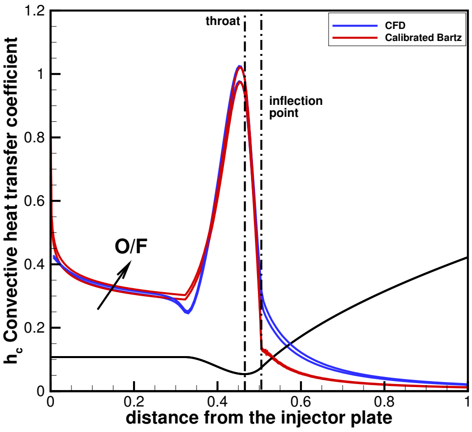

(c) Mixture ratio variation.

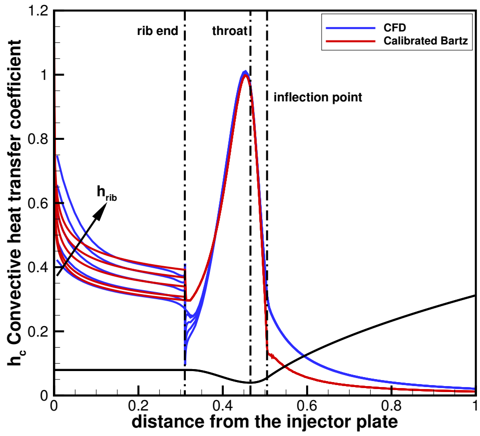

(d) Rib height variation.

Figure 9: Comparison between CFD numerical solution (Eq. 2), Bartz's heat transfer coefficient (Eq. 3) and its calibrated version (Eq. 6).

[3] Bartz, D. R., "Turbulent Boundary-Layer Heat Transfer from Rapidly Accelerating Flow of Rocket Combustion Gases and of Heated Air," Vol. 2 of *Advances in Heat Transfer*, 1965, pp. 1 – 108.

[4] Boldman, D. R., Schmidt, J. F., and Ehlers, R. C., *Prediction of local and integrated heat transfer in nozzles using an integral turbulent boundary layer*, National Aeronautics and Space Administration, 1972.

[5] Caisso, P., Souchier, A., Rothmund, C., Alliot, P., Bonhomme, C., Zinner, W., Parsley, R., Neill, T., Forde, S., Starke, R., Wang, W., Takahashi, M., Atsumi, M., and Valentian, D., "A liquid propulsion panorama," *Acta Astronautica*, Vol. 65, No. 11-12, 2009, pp. 1723 – 1737.

[6] Arione, L., Rudnykh, M., Tontini, R., Gurtovoi, A., Lobov, S., Shostak, A., Lillis, A. D., and D'Aversa, E., "The Status on the Development of LM10-MIRA LOX-LNG Expander Cycle Engine in the Frame of Lyra Program," *4th European Conference fro Aerospace Sciences, Bordeaux, France*, 2013.

[7] Strang, G., "On the Construction and Comparison of Difference Schemes," *SIAM Journal on Numerical Analysis*, Vol. 5, 1968, pp. 506–517.

[8] Brown, P., Hindmarch, A., and Byrne, G., "DVODE," *Computer Subroutine Package for Solving Ordinary Differential Equations*, Aug. 1992.

[9] Spalart, P. and Allmaras, S., "A One-equation Turbulence Model for Aerodynamic Flows," *La Recherche Aerospatiale*, Vol. 1, 1994, pp. 5–23.

[10] Kee, R., Rupley, F., Miller, J., Coltrin, M., Grcar, J., Meeks, E., Moffat, H., Lutz, A., Dixon-Lewis, G., and Smooke, M., "CHEMKIN Collection, Release 3.6, Reaction Design," *Inc., San Diego, CA*, 2000.

[11] Anderson, J. D., *Hypersonic and High-Temperature Gas Dynamics*, AIAA Education series, 2nd ed., 2006.

[12] Betti, B., Martelli, E., Nasuti, F., and Onofri, M., "Numerical Study of Heat Transfer in Film Cooled Thrust Chambers," 48^{th} AIAA/ASME/SAE/ASEE Joint Propulsion Conference & Exhibit, 29 Jul - 01 Aug 2012, Atlanta, GE. AIAA 2012-3907.

[13] Betti, B., Nasuti, F., and Martelli, E., "Numerical Evaluation of Heat Transfer Enhancement in Rocket Thrust Chambers by Wall Ribs," *Numerical Heat Transfer Part A: Applications*, Vol. 66, 2014, pp. 488–508.

[14] Betti, B., Pizzarelli, M., and Nasuti, F., "Coupled Heat Transfer Analysis in Regeneratively Cooled Thrust Chambers," *Journal of Propulsion and Power*, Vol. 30, 2014, pp. 360–367.

[15] Bianchi, D., Betti, B., Nasuti, F., and Carmicino, C., "Numerical Modeling of GOX/HTPB Hybrid Rocket Flowfields and Comparison with Experiments," *Journal of Propulsion and Power, in press*, 2014.

[16] Frassoldati, A., Cuoci, A., Faravelli, T., Ranzi, E., Candusso, C., and Tolazzi, D., "Simplified kinetic schemes for oxy-fuel combustion," 2009, pp. 6–10, 1^{st} International Conference on Sustainable Fossil Fuels for Future Energy, Rome, Italy.

[17] Betti, B., Bianchi, D., Nasuti, F., and Martelli, E., "Chemical Reaction Effects on Wall Heat Flux in Liquid Rocket Thrust Chambers," July 2014, 50^{th} AIAA/ASME/SAE/ASEE Joint Propulsion Conference & Exhibit, 28 - 30 Jul 2014, Cleveland, OH. AIAA 2014-3675.

[18] McBride, B. J. and Gordon, S., "Computer Program for Calculation of Complex Chemical Equilibrium Compositions and Applications," Tech. Rep. 1311, 1994, NASA Reference Publication.

[19] Roache, P. J., "Verification of Codes and Calculations," *AIAA Journal*, Vol. 36, No. 5, May 1998, pp. 696–702.

[20] Bray, K. N. C., "Atomic recombination in a hypersonic wind-tunnel nozzle," *Journal of Fluid Mechanics*, Vol. 6, No. 01, 1959, pp. 1–32.

[21] Bartz, D. R., "A Simple Equation For Rapid Estimation of Rocket Nozzle Convective Heat Transfer Coefficients," *Jet Propulsion*, Vol. 27, No. 1, 1957, pp. 49–51.

[22] Pavli, A. J., Curley, J. K., Masters, P. A., and Schwartz, R., "Design and Cooling Performance of a Dump-Cooled Rocket Engine," Tech. rep., DTIC Document, 1966.

[23] Kirchberger, C., Hupfer, A., Kau, H., Soller, S., Martin, P., Bouchez, M., and Dufour, E., "Improved prediction of Heat Transfer in Rocket Combustor for GOX/Kerosene," 47^{th} AIAA Aerospace Sciences Meeting Including The New Horizons Forum and Aerospace Exposition, 5-8 January 2009, Orlando, FL. AIAA 2009-1214.

[24] Krueger, R. C. and Curren, A. N., *Some factors influencing heat transfer to liquid-propellant rocket-thrust-chamber coolant channels*, Vol. 3671, National Aeronautics and Space Administration, 1965.

[25] Schacht, R. L. and Quentmeyer, R. J., *Axial and Circumferential Variations of Hot-gas-side Heat-transfer Rates in a Hydrogen-oxygen Rocket*, National Aeronautics and Space Administration, 1971.